

Saturation-Induced Instability and Its Avoidance in Adaptive Control of Hard Disk Drives

Néstor O. Pérez-Arancibia, *Member, IEEE*, Tsu-Chin Tsao, *Senior Member, IEEE*, and James S. Gibson, *Member, IEEE*

Abstract—This paper presents an investigation of the design and implementation of minimum-variance adaptive controllers for computer hard disk drive (HDD) read-write track following. A common characteristic of minimum-variance controllers, adaptive or not, is that they rely on prediction filters with large high-frequency gains to predict broadband disturbances, and this often produces control-signal saturation and eventual loss of stability. Two methods are introduced here to address this issue. The first method, suitable for online adaptive control, uses frequency weighting to constrain the high-frequency gain of the prediction filter. The second method, suitable for tuning fixed-gain controllers, employs an adaptive scheme iteratively over a finite duration. Both methods were implemented on a commercial hard disk drive, and experimental results demonstrate their effectiveness.

Index Terms—Control-signal saturation, frequency weighting, hard disk drive (HDD), iterative adaptive tuning, minimum-variance adaptive control.

I. INTRODUCTION

IN THE technical literature on *hard disk drives* (HDDs), two renowned control problems have been defined: track-seeking and track-following. The former deals with the motion control of the HDD heads between tracks in minimum time, the latter with maintaining the HDD heads on the center of the tracks. In this paper, we focus on track-following control of a commercial HDD.

It has been reported that track-following can be thought of as an output disturbance rejection problem [1]–[5], in which there exist two main sources of disturbances affecting the HDD dynamics. The first is *repeatable runout* (RRO), which is produced by imperfections and eccentricities on the tracks and characterized as being composed of sinusoidal signals with frequencies that are multiples of the HDD platters rotation frequency. The second is *nonrepeatable runout* (NRRO), produced by the ag-

gregated effects of disk drive vibrations, electrical noise in the circuits and the measurement channels.

Model-based minimum-variance adaptive schemes are well suited to deal with output disturbance rejection problems. Among the most prominent are the *adaptive inverse control* (AIC) [6] and the *adaptive-Q control* (AQC) [7] schemes. The former is particularly popular in the field of signal processing, where it was developed for noise-canceling applications [6]. The latter is derived from the notion of *Q*-parametrization, used to characterize the class of all stabilizing controllers [7], [8]. It can be shown that, despite the different denominations, AIC is a particular case of AQC. Studies on the design and implementation of add-on adaptive controllers for HDD track-following, resembling the AIC scheme, are reported in [1]–[3]. In those works, the adaptive control algorithm employs the classical *recursive least-squares* (RLS) method in [9]. The experimental implementation of an AQC scheme for HDD control, using the inverse QR-RLS algorithm in [10], is demonstrated in [5]. There, the disk drive open-loop plant is stabilized using a time-invariant *linear quadratic Gaussian* (LQG) compensator, and then, an adaptive *finite-impulse response* (FIR) filter *Q* is added according to the AQC configuration in [7]. In this paper, we approach the problem using an AIC-like minimum-variance adaptive control scheme, employing the inverse QR-RLS algorithm in [10].

A common characteristic of minimum-variance controllers, adaptive or not, is that they amplify low-level high-frequency disturbance while minimizing the mean-square values of the output errors. This results from the fact that such controllers rely on prediction filters with large high-frequency gains to predict broadband disturbances. In some applications, like those presented in [11]–[13], in the context of laser-beam jitter control, this amplification results in a spiking phenomenon in the control error, produced by the combination of control-signal saturation and amplified high-frequency disturbance. There, it is explained that in cases when the saturation is severe, spikes might be large enough, such that, the system output signal would take values outside of the sensor range, driving the system unstable. In the context of HDD control, the phenomenon of prediction filters with large high-frequency gains has been reported in [14]. There, it is argued that, in combination with poor plant identification, filters with large high-frequency gains might drive the adaptive system unstable. However, in that work, the specific mechanism explaining instability seems to be other than saturation, since this is not mentioned as a cause, and spiky behavior is not reported.

Manuscript received June 27, 2008; revised November 17, 2008. Manuscript received in final form March 12, 2009. First published September 01, 2009; current version published February 24, 2010. Recommended by Associate Editor G. Guo. This work was supported in part by the Office of Naval Research under Grant N00014-07-1-1063 and in part by the National Science Foundation Center for Scalable and Integrated Nanomanufacturing (SINAM) under Grant DMI-0327077 and Grant CMMI-0751621.

The authors are with the Mechanical and Aerospace Engineering Department, University of California, Los Angeles, CA 90095-1597 USA (e-mail: nestor@seas.ucla.edu; nestor_p_a@yahoo.com; ttsao@seas.ucla.edu; gibson@ucla.edu).

Color versions of one or more of the figures in this paper are available online at <http://ieeexplore.ieee.org>.

Digital Object Identifier 10.1109/TCST.2009.2018298

The concept of *strictly positive real* (SPR)¹ transfer function has been used extensively in the stability analysis of a general type of nonlinear systems, including a large number of adaptive ones. In particular, the notion of SPR transfer function is employed to establish stability and convergence of adaptive identification methods [17], [18], upon which several kinds of adaptive controllers are based on. For example, the scheme in [3] adaptively identifies an ARMAX model of the system's plant in where stability and convergence are demonstrated by assuming that the disturbance transfer function associated with the to-be-controlled system satisfies a SPR property. Thus, one could suspect that some of the problems mentioned in the previous paragraph are due to the fact that some SPR condition is not satisfied. However, that is not relevant in the control scheme considered in this work, because the system's plant is identified offline and what is computed adaptively is a minimizing filter that is chosen to be FIR. Therefore, SPR conditions are not explicitly required.

A well-known phenomenon in adaptive control systems is the appearance of a kind of instability called parameter drift [17], characterized by adaptive parameters going to infinity with time. This is due to the absence of *persistence of excitation* (POE) [9], [17], which occurs when the regressor vector employed for estimating the adaptive parameters is not rich enough in frequency content. Another common problem noted in the adaptive filtering and control literature is that the classical RLS algorithm might suffer from numerical instability when implemented in finite precision arithmetic. In the experiments presented here, instability associated with adaptive parameters taking large values is observed. However, compelling evidence is given supporting the idea that, in this case, the observation of adaptive gains growing to large values cannot be equated with parameter drift and lack of convergence, or with the numerical problems of the RLS algorithm. In fact, we show empirically using a numerically reliable algorithm, that in the HDD system considered here, the adaptive gains grow to large values because the steady-state theoretical optimal solution is composed of gains with large values, and not because there is parameter drift. The steady-state theoretical optimal solution is found by solving a Wiener–Hopf problem, employing *linear time-invariant* (LTI) identified disturbance models under the assumption that the disturbance affecting the system is statistically stationary.

Furthermore, this paper shows that, similarly to the cases studied in [11]–[13], in this study, adaptive prediction filters with large high-frequency gains produce signal saturation, resulting in the appearance of spikes in the position error signal and eventually in saturation-induced instability. To further test the notion that, in the HDD system considered here, the spiky behavior and instability are saturation-induced and not the result of parameter drift, we experimentally reproduce both phenomena employing LTI high-gain prediction filters.

In order to eliminate the saturation problem, two methods are presented here. The first method employs frequency weighting to reduce the value of the high-frequency gain of the adaptive prediction filter used to generate the control signal. The

¹There exists a close relationship between the concepts of *passivity* and SPR transfer function. For a complete treatment refer to [15], [16]. For a concise description see [17].

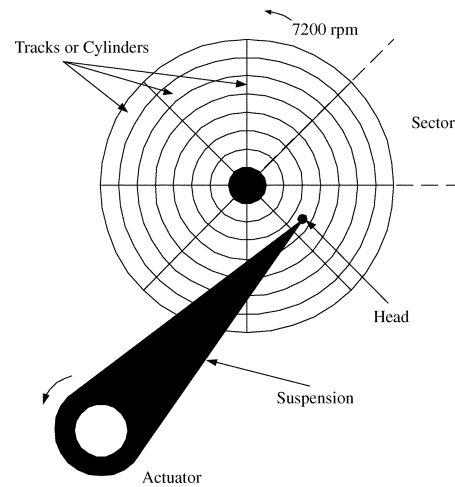


Fig. 1. Schematic idealization of the HDD system.

frequency response of both, experimentally obtained and analytically computed, steady-state filters demonstrate that, by using the frequency weighting method, the adaptive filter high-frequency gain can be reduced significantly, avoiding saturation-induced instability. The second method employs the original adaptive scheme iteratively over a finite duration to tune LTI minimum-variance controllers with reduced high-frequency gain prediction filters. This method is especially suitable for generating a series of fixed-gain controllers with increasingly better performance.

The paper is organized as follows. Section II presents the experimental setup and explains some relevant practical issues relating to the real-time implementation of the controllers. Section III describes the modeling and system identification of the plants involved in the experiments and considered in the analytical developments. Section IV explains the minimum-variance adaptive control scheme. Section V discusses the main experimental issues in the implementation of the adaptive loop. Section VI and Section VII discuss the frequency-weighted adaptive control method and the iterative adaptation method, respectively. Finally, Section VIII summarizes the main experimental results and Section IX condenses the main conclusions of this work.

II. DESCRIPTION OF THE EXPERIMENT

A hard disk drive is a mechatronic device that uses rotating platters to store data. Information is recorded on and read from concentric cylinders or tracks by read-write magnetic transducers, called heads, that fly over the magnetic surfaces of the HDD platters. The position of the heads over the platters is changed by an actuator that consists of a coil attached to a link, which pivots about a ball bearing. This actuator connects to the head by a steel leaf called the suspension [19], [20]. In the jargon of the HDD literature the moving part of the actuator is known as the *voice coil motor* (VCM). This description of the HDD is shown in Fig. 1.

The track-following control objective is to position the center of the head over the center of a data track, being the deviation of the center of the head from the center of a given track, often called *track misregistration* (TMR) [20], the typical measure of

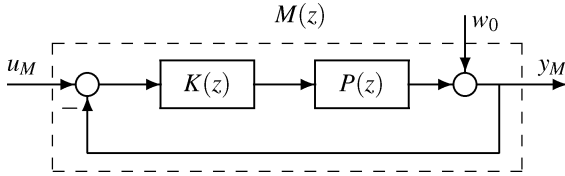


Fig. 2. Block diagram of closed-loop system M with PD feedback control. P : Open-loop plant; K : Classical PD feedback controller; $M = y_M/u_M = PK(1 + PK)^{-1}$, with y_M : Position of the HDD head, u_M : Excitation for system identification and w_0 : Output disturbance.

HDD tracking performance. A common index to quantify TMR is

$$\text{TMR} = 3\sigma \quad (1)$$

where σ is the empirical *standard deviation* (STD) of the control error signal. It is common to express 3σ as a percentage of the track pitch [20], which must be less than 10% in order to be considered acceptable. TMR values larger than this figure will produce excessive errors during the reading and recording processes.

In the experiments, we use a 2-platter (10 GB/platter) 4-head 7200 r/min commercial HDD, and a *Mathworks* xPC Target system for control. The sample-and-hold rate of 9.36 kHz, used for communication, control and filtering, is internally determined by the hard disk and transmitted through a clock signal to the target PC used for control. Both systems must operate in a synchronized manner. The position of a given HDD head over a platter is digitally transmitted by the use of two signals. The first conveys the *track number* (TN) over where the head is positioned. The second is the so-called *position error signal* (PES), which conveys the position of the head on the track pitch. Thus, the measured position is function of both the TN signal and the PES. The range of the PES is $[-0.5, 0.5]$ with a quantization-set size of 256, and where 0.0 corresponds to the center of the track. Notice that oftentimes the PES and the control error signal are identical.

III. PLANT MODELS AND SIGNALS

A. Identification of the Open-Loop Plant

The open-loop plants of single-stage actuated HDDs reflect the dynamics of their VCMs, which resemble the ones of double integrators or other similar low-pass-filter-type systems. In the context of track-following control, the dynamics of HDDs have been described extensively. Among many other works, we can mention [21]–[25]. Here, the open-loop plant of the system is denoted by P . An LTI model of P , denoted by \hat{P} , is obtained by system identification. Since the system is slightly damped, the system identification of P is performed in closed-loop employing the LTI controller K connected to P in the classical negative feedback configuration, as shown in Fig. 2, resulting in the closed-loop plant M given by

$$M = PK(1 + PK)^{-1}. \quad (2)$$

In this case, we choose to employ an *indirect* identification method [26], because the excitation signal u_M to the closed-loop plant M can be chosen to be independent of the disturbance

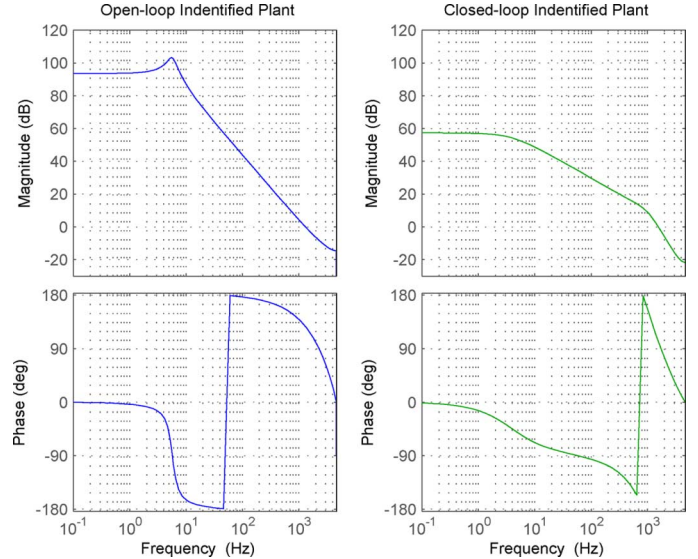


Fig. 3. *Left Plot*: Bode plot of the identified open-loop plant \hat{P} . *Right Plot*: Bode plot of the identified closed-loop plant \hat{G} .

signals affecting the open-loop plant P . Thus, first an estimate of the closed-loop plant M , denoted by \hat{M} , is found, and then \hat{P} is computed as

$$\hat{P} = \hat{M} [K(1 - \hat{M})]^{-1}. \quad (3)$$

Before performing the system identification of P , a plant model is not available, therefore, K is chosen to be a PD controller that is tuned on-line. Thus, after selecting suitable gains for K , a 20th-order closed-loop plant model \hat{M} is estimated using the *nAsid* subspace algorithm [27] from 40 000 input-output data points. This yields an open-loop plant model which is reduced to a 2nd order model after performing a balanced truncation. The resulting \hat{P} is shown on the left in Fig. 3. It is important to remark that the controller K and the plant M are employed in the identification of the open-loop plant only, and they are not mentioned in the rest of this paper.

B. Closed-Loop System With LTI Feedback Control

In order to robustly stabilize the slightly damped dynamics of the HDD, and also to maintain the HDD head over a chosen track, we first design an LTI controller. The LTI feedback control loop is shown in Fig. 4. The classical digital controller C consists of an integrator and a notch filter. The integrator gain and notch parameters were tuned to maximize the disturbance-rejection bandwidth and to force the HDD head to stay on a desired track. The input u in Fig. 4 will become the adaptive control command, and the output y is the position of the head's center over a given HDD platter. The output disturbance signal w_0 represents the combined effect of all the disturbances acting on the system, and the signal y_{ref} is the reference signal that the HDD head must follow. The closed-loop LTI system in the top diagram in Fig. 4, without \tilde{y} , can be represented as in the bottom diagram in Fig. 4 with

$$G = P(1 + PC)^{-1} \quad (4)$$

$$w = (1 + PC)^{-1}(w_0 + PCy_{\text{ref}}). \quad (5)$$

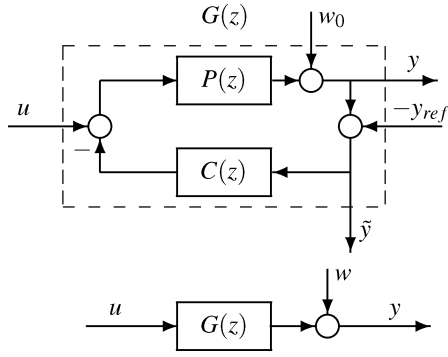


Fig. 4. *Upper Diagram*: Block diagram of the LTI feedback control system. *Bottom Diagram*: Equivalent model with $w = (1 + PC)^{-1}(w_0 + PC y_{ref})$.

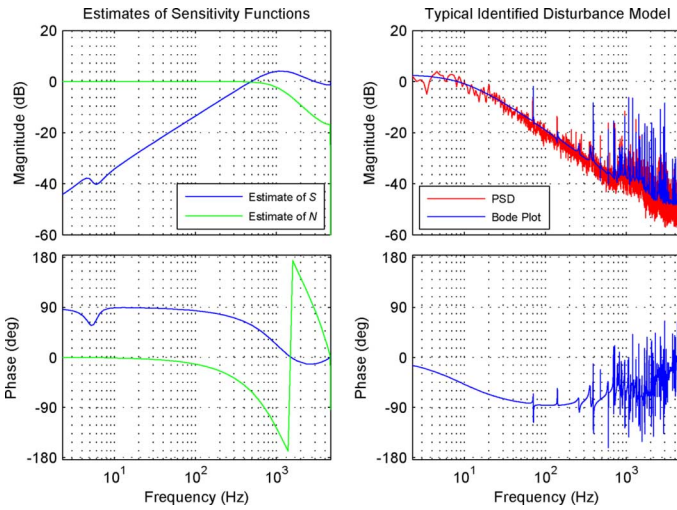


Fig. 5. *Left Plot*: Estimates of the sensitivity functions, \hat{S} and \hat{N} . *Right Plot*: Bode plot of a typical identified model W_1 . The Bode plot of W_1 is compared with the spectrum of the experimental signal w_1 plotted in red.

The closed-loop plant dynamics were reidentified by the aforementioned subspace method and labeled as \hat{G} . The Bode plot of \hat{G} is shown on the right in Fig. 3. The output and complementary sensitivity functions, S and N , of the closed-loop LTI system are

$$S = y/w_0 = (1 + PC)^{-1} \quad (6)$$

$$N = y/y_{ref} = PC(1 + PC)^{-1}. \quad (7)$$

An estimate of S , computed as $\hat{S} = (1 + \hat{P}\hat{C})^{-1}$, is shown in blue on the left in Fig. 5. Because the gain of the controller C was chosen to maximize the error-rejection bandwidth, the LTI loop amplifies high-frequency disturbance above about 200 Hz. Also, an estimate of the complementary sensitivity function N , computed as $\hat{N} = \hat{P}\hat{C}(1 + \hat{P}\hat{C})^{-1}$, is shown in green on the left in Fig. 5. This plot shows that for a constant signal y_{ref} , we can consider $y = N y_{ref}$.

C. Disturbance and LTI Disturbance Models

The use of disturbance models has been recently reported to be useful for analyzing the steady-state behavior and theoretical performance of minimum-variance adaptive control sys-

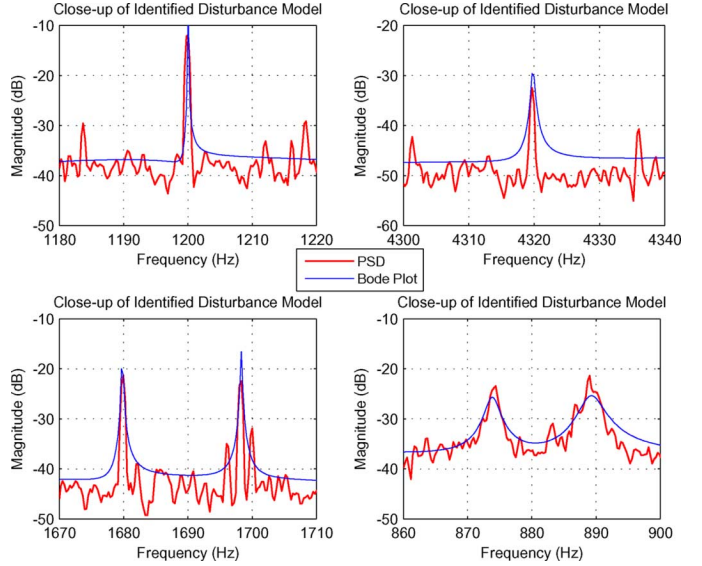


Fig. 6. Close-ups of the upper-left plot in Fig. 5. Using linear scale, these plots show some spikes and narrow-band peaks over frequency (Hertz). The upper plots show close-ups of two spikes at frequencies that are multiples of 120 Hz. The bottom plots show the close-ups of narrow-band peaks at frequencies that are not multiples of the HDD platters rotation frequency.

tems [13], when the disturbance acting on the system is statistically stationary. The main idea is that stationary stochastic disturbances affecting the system dynamics can be modeled as outputs from finite-dimensional stable LTI systems excited by white sequences with zero mean.

Besides u , the input signals driving the system are w_0 , which can be considered stochastic, and y_{ref} , which is a deterministic signal, often taking a constant value. The output of main importance here is \tilde{y} , which contains all the information used to tune the adaptive controller. The sequences w_0 and y_{ref} are independent. Subsequent analysis uses the sequences

$$w_1 = (1 + PC)^{-1}w_0, \quad r_1 = PC(1 + PC)^{-1}y_{ref}. \quad (8)$$

The adaptive controller in Fig. 8, in the next section, implicitly identifies certain statistics of \hat{w} but otherwise requires no information about any of the sequences in (8). For theoretical analysis of the performance of the adaptive controller, here, we assume that the sequence w_0 in (8) is stationary with zero mean. Also, the analysis assumes the disturbance models

$$w_0 = W_0\varepsilon_w, \quad w_1 = W_1\varepsilon_w \quad (9)$$

where W_0 and W_1 are finite-dimensional stable LTI filters, and the sequence ε_w is independent, stationary, white and zero mean with

$$E\{\varepsilon_w^2(\cdot)\} = 1. \quad (10)$$

Notice, that $W_1 = SW_0$ and that W_0 and W_1 can be interpreted as open-loop and closed-loop disturbance models, respectively. It must be emphasized that none of these models are needed for implementing the adaptive controller. The disturbance model W_1 is required for estimating the theoretical optimal steady-state gains in the adaptive controller and the corre-

of the adaptive controller appreciably, so that, it can be stated that by minimizing (16) the performance index

$$J_{\tilde{y}}(F) = \text{RMS}(\tilde{y}) = \sqrt{E\{\tilde{y}^2(\cdot)\}} \quad (18)$$

is approximately minimized as well. This argument can be formalized using the discrete-time swapping lemmas in [17].

For the disturbance model of w_1 discussed in Section III, the sequence ε_w is white with unit variance. Then, it follows from Fig. 8 that the steady-state tuning and error signals, e and \tilde{y} , satisfy

$$e = \tilde{y} = (1 + F\hat{G})W_1\varepsilon_w \quad (19)$$

which implies that the steady-state RMS values of these signals, for a given F , can be calculated as

$$J_e(F) = J_{\tilde{y}}(F) = \left\| (1 + F\hat{G})W_1 \right\|_2. \quad (20)$$

In steady-state, the adaptive control loop minimizes $J_e(F)$ over the set of FIR filters of order L . In order to write (20), we assume that the LTI model W_1 is able to capture completely the statistical information contained in w_1 . For the purpose of theoretical analysis, with the assumed disturbance model and condition (11), the minimization of $J_e(F)$ over FIR filters of order L can be formulated as a Wiener–Hopf problem [29]. A method for finding the minimizing F for the indices in (20) is developed in Appendix I.

B. Adaptive Tuning

In many applications, an important reason for employing adaptive control systems for disturbance rejection is that disturbance statistics often change with time. However, even if w_0 remains stationary, the scheme in Fig. 8 is an appropriate option, because it can be employed for tuning an LTI filter F . In principle, the system can be allowed to adapt until the filter gains f_l converge to their optimal values. However, for reasons that will become clear in the next section, in the experiments discussed here, it is more desirable to adapt the filter for a finite duration only, since if the adaptive system is run indefinitely, it would eventually become unstable.

In this subsection, we describe an adaptive tuning experiment that gives us some crucial keys in the development of solutions for the stability problems to be discussed in the next section. Using the system in Fig. 8, the filter F is adapted for 20 s, employing the inverse QR-RLS algorithm with a forgetting factor of 0.999999. When using this algorithm as defined in [10], the speed of adaptation depends on the initialization parameter ε . For example, in experiments over the track 15 000 of head 0, for $\varepsilon = 10^{-6}$, the system adapts slowly. The experiments summarized in Table I were conducted over that HDD location with the same value of ε .

From an LTI viewpoint, a reason for stopping the adaptation after 20 s of tuning is that the resulting filter achieves a performance very close to the theoretical optimal one, computed as in the previous subsection, but with one desirable property that is shown in Table I. There, the main thing to notice is that, for tuned filters with $L = 6$ and $L = 36$, the values of $\|F\|_1$ and $\|F\|_\infty$ are considerably smaller than the values of $\|F\|_1$

TABLE I
COMPARISON OF FILTERS

	Theoretical	Experimental (20 s)
$3\sigma, L = 6$	4.78	5.14
$\ F\ _\infty, L = 6$	16.39	1.86
$\ F\ _1, L = 6$	16.39	2.58
$3\sigma, L = 36$	4.36	4.96
$\ F\ _\infty, L = 36$	20.52	2.73
$\ F\ _1, L = 36$	33.28	5.08

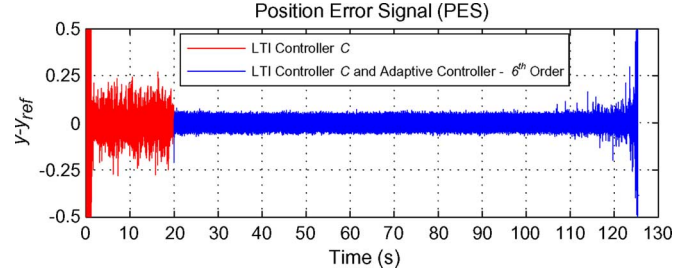


Fig. 9. Time series from experiment using the scheme in Fig. 8, with $H = 1$. The adaptive filter F has order 6. Notice that between Time = 100 s and Time = 110 s, spikes begin to appear in the *position error signal* (PES). The experiment was performed on track 15 000 of head 0.

and $\|F\|_\infty$ corresponding to the analytically computed optimal filters. For example, for the case $L = 6$, the 20-s adaptively tuned filter achieves a 3σ performance that is only 7.53% higher than the theoretical optimal one for the same L , while its H_∞ norm is 8.81 times smaller. Similar results were obtained for different values of L over several different tracks. This property will be demonstrated to be useful in order to avoid problems such as control-signal saturation and loss of stability robustness to model uncertainty, while maintaining high performance.

V. EXPERIMENTAL ISSUES IN THE IMPLEMENTATION OF THE ADAPTIVE LOOP

A. Trajectory of the Adaptive Gains

The purpose of this section is to show and explain the loss of stability of the HDD system when under the control scheme in Fig. 8 with $H = 1$. One might suspect, that this phenomenon reflects lack of convergence of the adaptive scheme and parameter drift due to the absence of POE [17]. However, the review of recent experimental and analytical studies [11], [13] suggests that this undesirable phenomenon might be associated with the high-frequency high gain of the steady-state optimal filter to which the adaptive filter F tends to converge, which might cause control-signal saturation and eventual loss of stability.

In order to test the hypothesis proposed in the previous paragraph, the system in Fig. 8, with $H = 1$, is allowed to adapt until the HDD head swerves out of control, while monitoring the evolution of the filter parameters. In Fig. 9, we show the time-series of the PES for this experiment with the filter F adapting slowly (initialization parameter $\varepsilon = 10^{-6}$ as defined in [10]). The first observation to make is that the system achieves an excellent performance in fractions of a second, even though, the filter gains

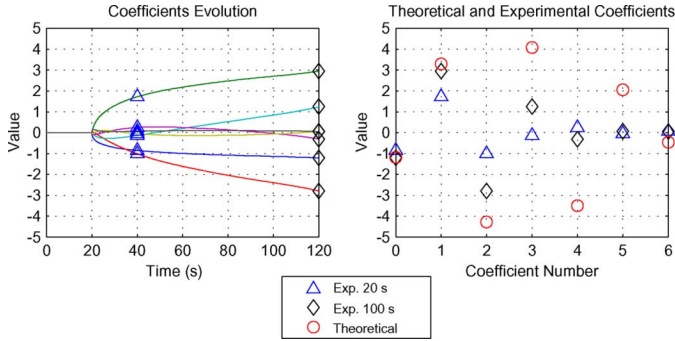


Fig. 10. Evolution of filter gains f_l over time. The theoretical optimal gains are marked with red circles. The gains tuned for 100 s are marked with black diamonds. The gains tuned for 20 s are marked with blue triangles. Notice that all the black diamonds lie between the blue triangles and the red circles. The experiment was performed on track 15 000 of head 0.

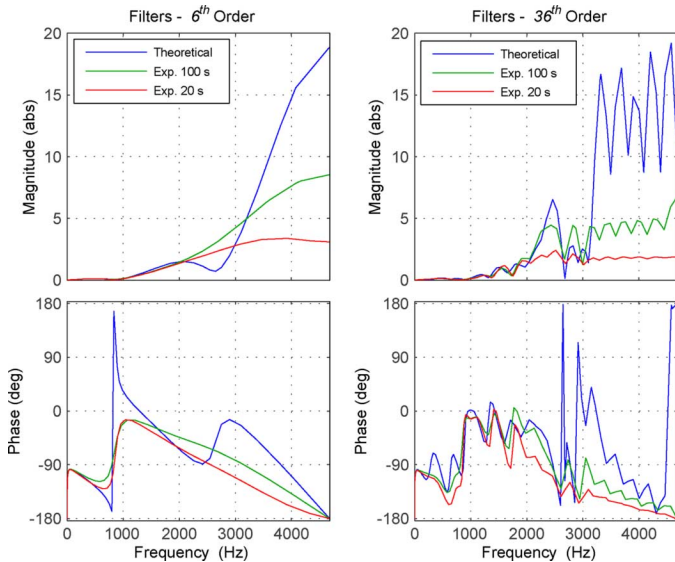


Fig. 11. Comparison of tuned filters (for 20 and 100 s) with the theoretical computed one. *Left Plot:* 6th-order filters. *Right Plot:* 36th-order filters.

are far away from reaching their theoretical optimal values, as shown in Fig. 10, ratifying the results in Table I.

Another observation to make is that several seconds before the HDD head is drifted out of the track, spikes begin to appear in the PES. This is of particular interest, because in the works reported in [11] and [13], it was shown that spikes might appear in the position error as the result of a combination of control-signal saturation and filters F with large gains over the high-frequency range. Thus, Fig. 9 suggests that the instability appearing during the adaptation process is not related to parameter drift, but due to the fact that the steady-state optimal filter F has a large gain over the high-frequency range. This idea is supported by Figs. 10 and 11.

In Fig. 10, we show the trajectory of the gains f_l during adaptation, with $L = 6$. There, it is clear that the filter gains are moving in the correct direction toward the points marked with the symbol \circ , which indicate the positions of the theoretical steady-state optimal gains f_l computed by minimizing (20) using the method in Appendix I. With the symbols \triangle and \diamond ,

we mark the positions of the gains f_l adapted for 20 and 100 s, respectively. For each gain, the symbol \diamond lies in between the symbols \triangle and \circ , which demonstrates that the adaptive gains are following the desired trajectory from \triangle to \circ . The same behavior was observed in the case $L = 36$. The coefficients evolution plot for $L = 36$ is omitted. The resulting filters are shown on the right in Fig. 11.

Considering the evidence given in the previous paragraphs, we infer that the instability observed in Fig. 9 is caused by the large values that the adaptive filter F gains take, and that this is not related to problems in the adaptive algorithm. The proposed specific mechanism is as follows. The spikes in the PES appear as the result of signal saturation. As the filter gains f_l grow toward their steady-state optimal values, the amplitudes of the spikes in the PES also grow, and the predicted signal \hat{w} in Fig. 8, estimated using the LTI model \hat{G} , becomes increasingly less accurate. Thus, after some seconds, this process produces spikes in the PES with amplitudes large enough, such that, the HDD head is drifted out of the track. When this occurs, the information used to tune the adaptive filter F becomes completely erroneous, driving the system unstable. To further test these ideas, we perform experiments in which the spiky and unstable behaviors are reproduced even when the adaptive filter F is replaced by a tuned LTI filter.

B. Control Signal Saturation

In [11], it was demonstrated that spikes might appear in the control error signal as the result of a combination of an adaptive filter F with high gain over the high-frequency range and control-signal saturation. In that work, the signal becoming saturated was the output u from the filter F in Fig. 8. In the experiments performed on the HDD with the results shown in Fig. 9, none of the signals generated inside the digital controller becomes saturated. Then, if the spikes appearing in Fig. 9 are produced by signal saturation, then the question is, which is this signal?

In order to elucidate this issue, we devise an experiment in which the adaptive filter F in Fig. 8 is replaced with the adaptively tuned LTI filter F_{90} , where the subindex 90 indicates that F_{90} is the filter adapted for 90 s as shown in Fig. 9 and Fig. 10. Notice that after 90 s, which corresponds to Time = 110 s in Fig. 9, the first spikes begin to appear in the PES. It is clear that replacing the adaptive filter F with the LTI system F_{90} is equivalent to defining

$$U_{90} = F_{90}(1 + \hat{G}F_{90})^{-1} \quad (21)$$

and then connecting the new LTI controller $C - U_{90}$ to the open-loop plant P , i.e., the system C is replaced with the system $C - U_{90}$ in the upper diagram of Fig. 4. The experimental results are shown in Fig. 12. As expected, spikes appear in the PES without driving the system unstable. This behavior can be explained by the block diagrams in Fig. 13. There, the upper block contains the saturation block Sat, which sets the value of the signal v_{sat} to $-\alpha$ or α when $|v(\cdot)| > \alpha$. At this point the existence of the saturation block is a matter of speculation, therefore, the value of α is unknown.

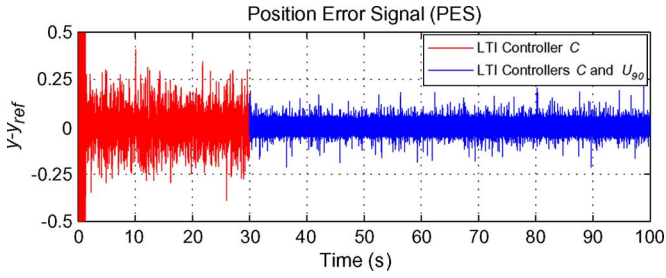


Fig. 12. Time series from experiment performed using the LTI controller \tilde{U}_{90} . Notice the presence of spikes in the PES.

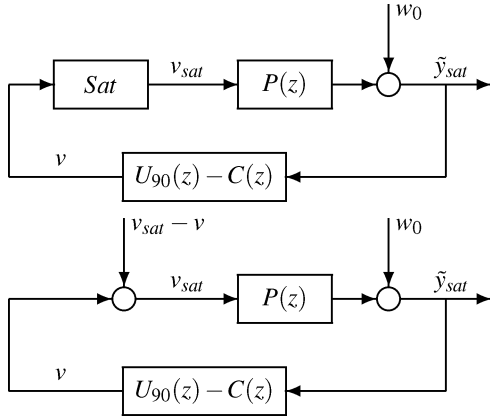


Fig. 13. *Upper Diagram*: Saturation model explaining spikes in time series in Fig. 12. *Bottom Diagram*: Equivalent model. Notice that the mapping from $v_{\text{sat}} - v$ to \tilde{y}_{sat} is the input sensitivity function I_{90} .

To test the idea that the spikes appearing in the PES are caused by saturation, first notice that the top and bottom block diagrams in Fig. 13 are equivalent, and that the mapping from $v_{\text{sat}} - v$ to \tilde{y}_{sat} is the input sensitivity function

$$I_{90} = P[1 + P(C - U_{90})]^{-1}. \quad (22)$$

Also, notice that given that the disturbance affecting the system has a significant amount of high-frequency content and that the prediction filter F_{90} has a high-pass shape, the signal v has a significant amount of high-frequency content as well. This indicates that similarly to the case presented in [11], the signal $v_{\text{sat}} - v$ is a signal composed of isolated impulses or sporadic group of impulses, and consequently many of the spikes in the PES should be isolated impulse responses of the system I_{90} . Thus, the obvious way to test our saturation hypothesis is to compare the shape of several spikes in Fig. 12 with the impulse response of the system I_{90} in (22). If in this comparison there are several spikes that resemble the shape of the impulse response of I_{90} , then, saturation affecting the signal v , as modeled in Fig. 13, would be the most reasonable explanation for the appearance of spikes in the PES. Empirical evidence supporting the saturation explanation is shown in Fig. 14. There, it can be observed that in these four cases, the spikes in the PES clearly resemble the shape of the impulse response of I_{90} , as expected. However, in many other spikes the resemblance is not that obvious. This slight discrepancy is explained by the fact that some spikes are not produced by a single impulse, but by a small group of consecutive impulses.

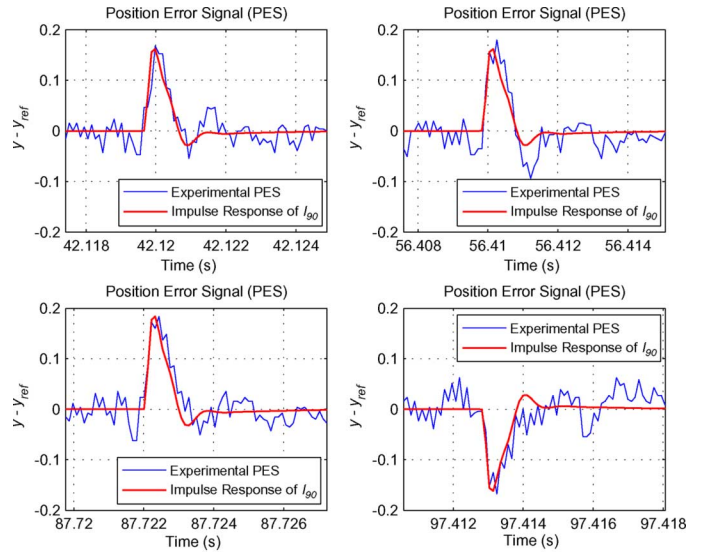


Fig. 14. Empirical evidence supporting the model in Fig. 13. Spikes from the time series in Fig. 12 are compared to the scaled impulse response of I_{90} .

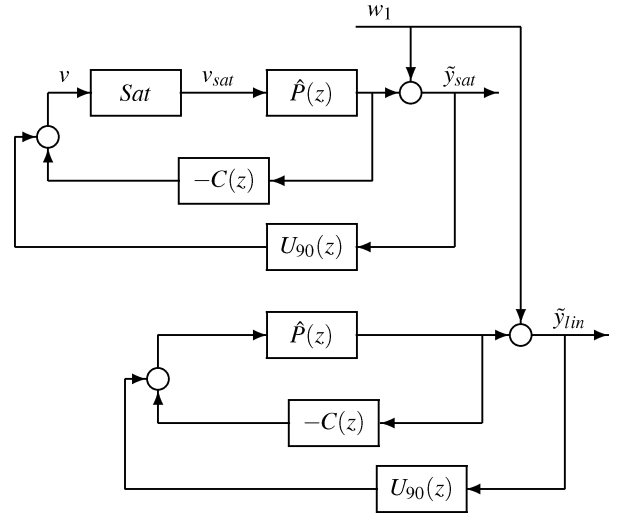


Fig. 15. Block diagram of simulations with LTI controller U_{90} . Block labeled *Sat* represents control saturation.

Considering the ideas and results in the previous paragraphs and given that in the experiment the signal v_{sat} is not available for measurement, we devised a simulation to illustrate the phenomenon completely. The simulation diagram is shown in Fig. 15. There, we use the LTI controllers C and U_{90} , we choose an arbitrary value of $\alpha = 0.1$ V, such that, spikes appear in the PES, and we use a disturbance signal w_1 , which is a sequence recorded from a real-time experiment.

The simulation results are summarized in Fig. 16. There, the left-upper plot compares the simulated linear and saturated position error signals. Notice that, as in the experimental PES in Fig. 12, spikes appear in the simulated saturated PES, while they do not appear in the simulated linear PES. The left-bottom plot compares the corresponding signals v and v_{sat} . To explain the appearance of spikes in the saturated PES, notice that, as predicted in the previous paragraphs, for this disturbance sequence w_1 , the controller $C - U_{90}$ generates a signal v with a significant high-frequency content so that $v_{\text{sat}} - v$ is composed of

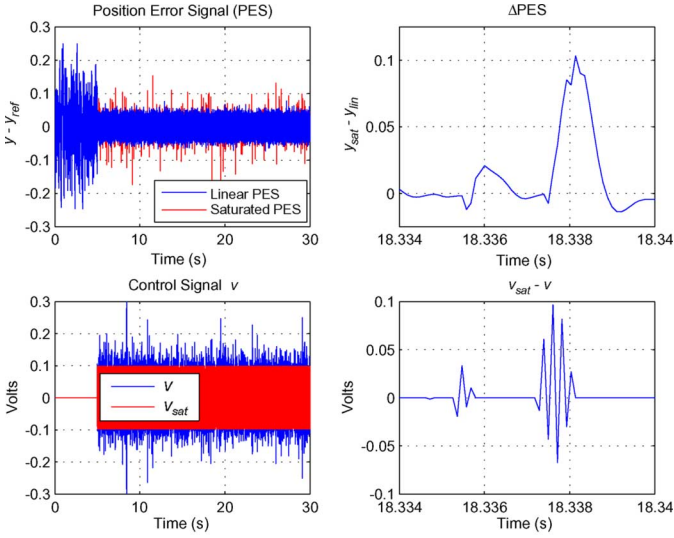


Fig. 16. Results from the simulations in Fig. 15. *Left-Upper Plot*: Simulated linear and saturated PES showing the nature of the spikes. *Left-Bottom Plot*: Signals v and v_{sat} from linear and saturated simulations. *Right-Upper Plot*: Close-up of the plot of ΔPES . *Right-Bottom Plot*: Close-up of the plot of the signal $v_{\text{sat}} - v$.

isolated impulses and sporadic groups of impulses as shown on the right-bottom side of Fig. 16, which is a close-up of the plot of $v_{\text{sat}} - v$. In order to show the absolute effect of $v_{\text{sat}} - v$ on the PES, a close-up of $\Delta PES = \tilde{y}_{\text{sat}} - \tilde{y}_{\text{lin}} = y_{\text{sat}} - y_{\text{lin}}$ is shown on the right-upper side of Fig. 16. Notice that ΔPES is exactly the output from I_{90} for the input $v_{\text{sat}} - v$. This explains the nature of the spikes appearing in the simulated saturated PES (signal \tilde{y}_{sat}).

Thus, taking into account the information provided by the previous experiments and simulations, the natural conclusion is that the spikes appearing in the position error shown in Fig. 9 can be explained by the saturation model in Fig. 13. A similar phenomenon has been observed in the optical experiments and simulations presented in [11]–[13], where the signal that saturates is the output from the filter F . In the case of HDDs, saturation can be explained as the direct consequence of the limited output range of the electronic circuits forming part of the controller-actuator interface. Nevertheless, in the spirit of the scientific method [30], if all the information that the experimenter has available is the plot in Fig. 9, then the connection between instability and saturation is not obvious, and consequently, such conjecture must be tested experimentally.

From a stability point of view it is fair to say that saturation, if it is severe enough, will drive the system unstable. As suggested by the experiments and simulations shown in this subsection, saturation results from filters F with large high-frequency gains, being this the ultimate cause of the instability shown in Fig. 9. However, assuming an LTI filter F , a natural question to ask is whether a relationship between the H_∞ norm of F and the classical indices of stability robustness, gain and phase margins, can be established. This issue is explored in the next subsection.

C. Stability Robustness From a Classical LTI Viewpoint

In this subsection, we look for a connection between prediction filters F with high-frequency high gains and loss of sta-

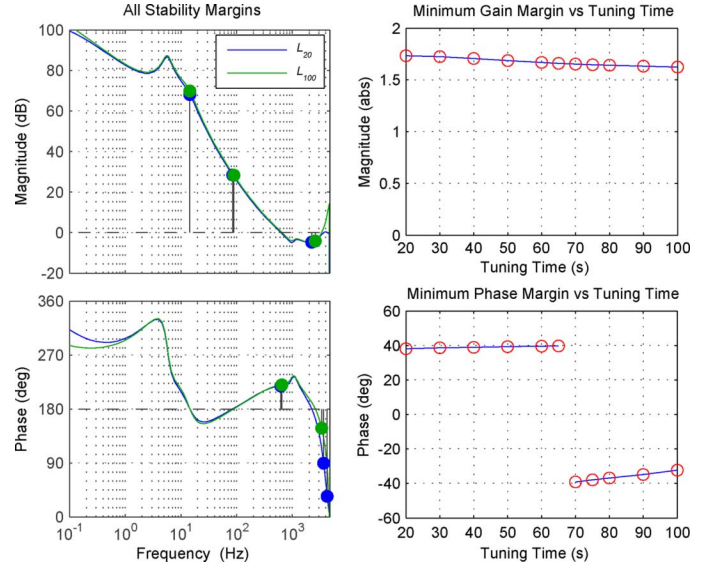


Fig. 17. *Left Plot*: Bode plot of the open-loop gains L_{20} and L_{100} , showing all stability margins. *Right Plot*: Minimum gain and minimum phase margins versus tuning time T . The discontinuity in the right-bottom plot is explained due to the fact that each of the loop gains L_T has several stability crossings.

bility robustness from a strict LTI viewpoint. In case that a clear connection was established between the both, the appearance of spikes in the position error and the loss of stability in the system would have an alternative explanation.

To begin with, we define

$$L_T = \hat{P}(C - U_T), \quad U_T = F_T(1 + \hat{G}F_T)^{-1} \quad (23)$$

with $T \in [20, 100]$ indicating the amount of time that the filter F_T has been tuned as shown in Fig. 10, using the scheme in Fig. 8. Notice that as shown in Fig. 11, the H_∞ norm of F_T grows along with T . The open-loop gain systems L_T are employed to compute gain and phase margins as functions of T . On the left in Fig. 17, we compare the open-loop gains L_{20} and L_{100} . The first characteristic to notice is the great similitude between the two Bode plots, which define very similar stability margins. This is counterintuitive because as shown in Fig. 11 the filters F_{20} and F_{100} have very different Bode plots.

On the right in Fig. 17, we show minimum gain and minimum phase margins of the closed-loop system as function of the tuning time T . Notice that, in this case, there is no clear connection between adaptation time and these classical *single-input–single-output* (SISO) LTI indices of stability robustness. The discontinuity in the right-bottom plot in Fig. 17 is explained due to the fact that each of the loop gains L_T has several stability crossings. For example, for L_{20} the minimum crossing angle is positive and for L_{100} the minimum crossing angle is negative.

The main conclusion from the analysis in the previous paragraphs is that the systems U_T , computed using the adaptively tuned filters F_T , define controllers $C - U_T$ that generate robustly stable closed-loop systems from an LTI viewpoint, and therefore, this kind of analysis loses relevance, even if F is LTI, when nonlinear phenomena, such as saturation, are present in the system. A different approach is attempted in the next subsection.

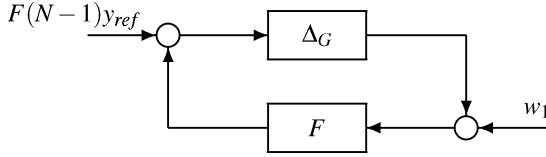


Fig. 18. Typical feedback connection.

D. A General Notion of Stability Robustness

Thus far, we have considered perfect matching between the physical system and the LTI identified model of the closed-loop plant, i.e., $\hat{G} = G$, which in general is unrealistic. Thus, for purposes of analysis, in this subsection, we consider additive uncertainty, i.e.,

$$G = \hat{G} + \Delta_G \quad (24)$$

where G is, for now, assumed to be LTI and therefore saturation and other nonlinearities are not present in the system. Then, it is clear that the upper part of the scheme in Fig. 8 can be put as shown in Fig. 18.

From an LTI viewpoint, we follow the following analysis. After convergence has been achieved, the filter F can be considered to be LTI. Also, it is clear that the scheme in Fig. 18 is well posed, therefore, a sufficient condition for BIBO stability is

$$\|\Delta_G\|_1 \|F\|_1 < 1. \quad (25)$$

Similarly, a sufficient condition for asymptotic stability is

$$\|\Delta_G\|_\infty \|F\|_\infty < 1. \quad (26)$$

These conditions suggest that filters F with smaller norms make the stability of the whole scheme more robust to additive uncertainty in the plant model \hat{G} . Notice that for the special case $\hat{G} = G$, the adaptive scheme is always stable as long as the norms of F remain bounded. Conditions (25) and (26) might seem rather conservative and unpractical. However, they reinforce the idea that filters F with high gains are undesirable, not only because they might produce saturation, but also because filters F with norms small enough make the control scheme robustly stable to plant model uncertainty.

Finally, it should be noted that the assumptions that F has converged and that G is LTI can be relaxed and the conditions in (25) and (26) remain essentially the same except for the replacement of $\|\cdot\|_1$ by $\|\cdot\|_{\ell_\infty \rightarrow \ell_\infty}$, defined as in [31], and the replacement of $\|\cdot\|_\infty$ by $\|\cdot\|_{\ell_2 \rightarrow \ell_2}$, defined as in [31]. This provides us with a more general notion of stability robustness and a better guideline for design.

VI. FREQUENCY-WEIGHTED ADAPTIVE CONTROL

Thus far, we have established a clear relationship between prediction filters F with high gain over the high-frequency range and the appearance of spikes in the PES due to saturation, and also, with loss of stability robustness, all which might eventually drive the system out of control. As we showed in Section IV, a way to deal with these problems is to tune an LTI filter F for a finite duration. This is reasonable because high performance can

be achieved with suboptimal filters as displayed in Table I. The problem with that approach is that we lose the adaptive capabilities of the scheme in Fig. 8, which could imply a noticeable performance degradation if statistical variations occurred in the disturbance signal w_0 in Fig. 4.

In [11], it was shown that the use of frequency weighting is an effective way to modify the frequency response of the theoretically computed steady-state prediction filter F , and therefore, modify the trajectory of the adaptively computed gains f_i . Here, frequency weighting is introduced by the use of a weighting filter H in the scheme shown in Fig. 8.

The frequency response of the steady-state F depends on the frequency content of the disturbance, as well as the plant transfer function. However, fundamentally, F predicts the disturbance, and prediction filters typically have large high-frequency gains. A way to see that is that the minimum-variance F is, in a certain sense, an approximate inverse of the plant transfer function G , which rolls off at high frequencies, as shown by the Body plot of \hat{G} in Fig. 3. In the adaptive control loop, a filter F with large high-frequency gain would amplify high-frequency disturbance and sensor noise, and increase the sensitivity of the closed-loop system to high-frequency modeling error in \hat{G} , creating the problems already studied in Section V.

The question then is, what type of weighting filter H will lead to an FIR filter F with reduced high-frequency gain? The somewhat counterintuitive answer is a high-pass filter H . The sense in which F inverts G is that F minimizes the H_2 -norm of $1 + F\hat{G}$ weighted by W_1 as in (20). Thus, it is clear that the incorporation of a high-pass H , as in Fig. 8, would penalize the high-frequency gain of F . When using the weighting filter H the tuning signal becomes He , and consequently the theoretical minimization index is

$$J_{He}(F) = \left\| H(1 + F\hat{G})W_1 \right\|_2 \quad (27)$$

which can be minimized employing the method in Appendix I, after replacing W_1 with HW_1 . Notice, that when using frequency weighting the theoretical performance is still given by $\|(1 + F\hat{G})W_1\|_2$ as in (20).

The selection of an adequate high-pass filter H is made heuristically. Thus, the parameters of H are treated as tuning parameters of the adaptive controller in Fig. 8. The tuning process can be performed using simulations in combination with experimental data, or by minimizing (27) with the use of an offline identified disturbance model W_1 . Here, H is an 8th-order FIR filter computed using standard digital filter design methods, where the main tuning parameter is the cutoff frequency of H . Thus, a graphical relationship can be drawn showing the tradeoff between the cutoff frequency of H and the 3σ performance index, as shown in the bottom plot of Fig. 21.

On the left in Fig. 19, we show the Bode plots of the theoretically computed optimal filters F employing high-pass weighting filters H with four different cutoff frequencies (no filter, 0.7, 1.0, and 1.3 kHz). There, the effectiveness of using frequency weighting can be clearly appreciated, since the filter gain over the high-frequency range is decreased dramatically. The plot on the right in Fig. 19 compares the theoretically computed and the experimentally obtained filters F employing

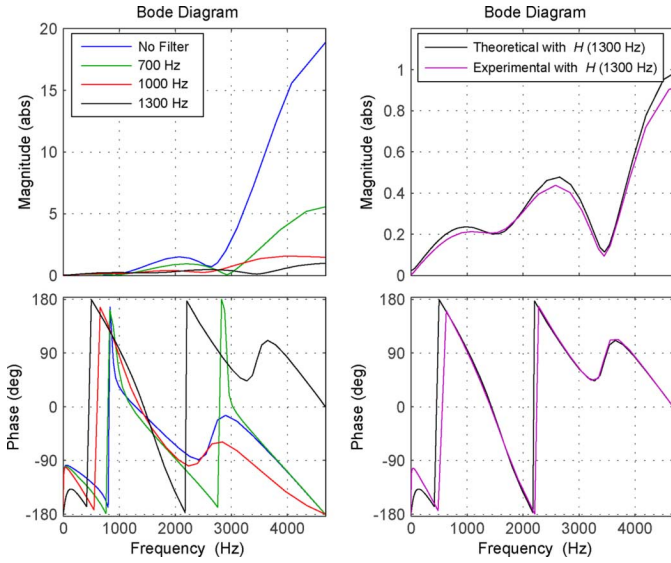


Fig. 19. *Left Plot*: Bode diagrams of optimal filters F theoretically computed using high-pass weighting filters H with different cutoff frequency (no filter, 700, 1000, and 1300 Hz). *Right Plot*: Comparison between theoretically computed and experimentally obtained filters F , with a weighting filter H with a cutoff frequency of 1300 Hz.

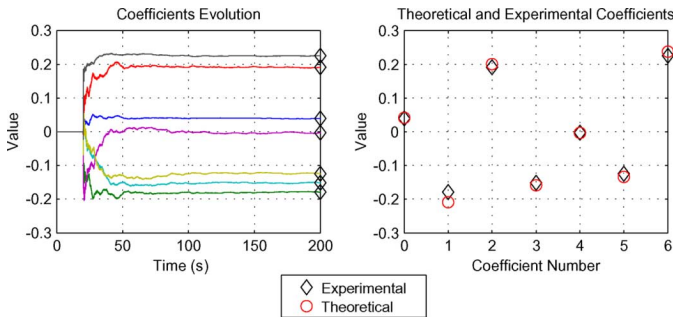


Fig. 20. Evolution of filter gains f_i over time. These gains were obtained from the experimental implementation of the frequency-weighting adaptive control method on track 15 000 of head 0, using a weighting filter H with a cutoff frequency of 1300 Hz.

a weighting filter H with a cutoff frequency of 1.3 kHz. The plots in Fig. 19 along with the plots in Fig. 20 demonstrate that by incorporating frequency weighting, the steady-state solution, to which the gains f_i converge, can be modified, making possible the implementation of the adaptive scheme in Fig. 8 in a robust manner and without running into problems such as control-signal saturation or loss of stability robustness. Notice, that in Fig. 20 the adaptive parameters f_i reach the steady-state values significantly fast. This is because the initialization parameter of the adaptive filter, ε , is set to 10^{-16} . The forgetting factor is the same that in the experiments presented in Section IV-B.

The use of frequency weighting implies a tradeoff between filter gain reduction and performance degradation. A study of how frequency weighting affects performance is summarized in Fig. 21. There, the upper plot shows the value of $\|F\|_\infty$ as function of the cutoff frequency of H , the middle plot shows the value of $\|F\|_1$ as function of the cutoff frequency of H , and the bottom plot shows the performance index 3σ as function of the cutoff frequency of H . In these three plots, the theoretical values

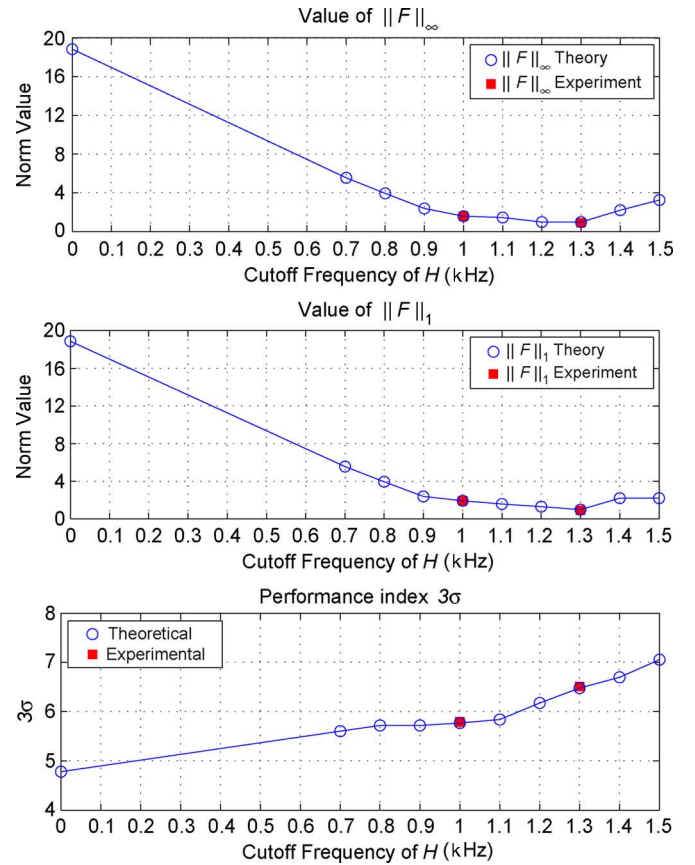


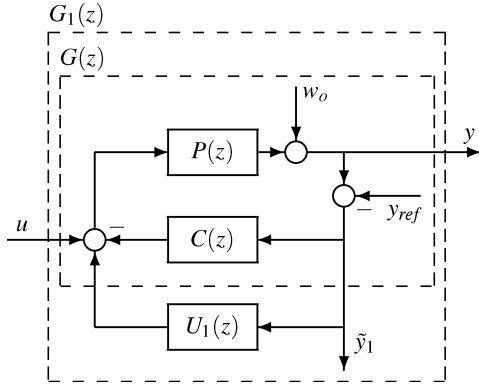
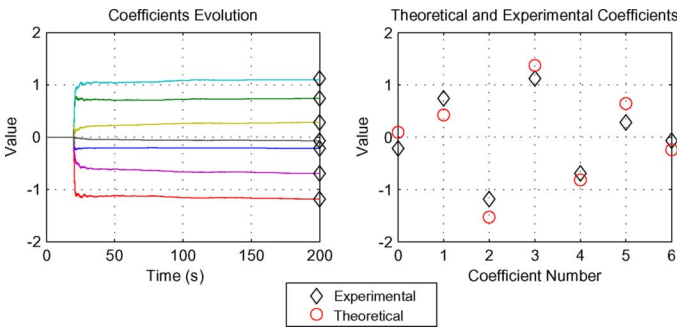
Fig. 21. *Upper Plot*: Value of $\|F\|_\infty$ as function of the filter H cutoff frequency. *Middle Plot*: Value of $\|F\|_1$ as function of the filter H cutoff frequency. *Bottom Plot*: Performance index 3σ as function of the filter H cutoff frequency.

are marked with blue hollow circles and the experimental values with solid red squares. These results show the dramatic filter norm reduction achievable with the use of appropriate weighting at the expense of some performance degradation.

VII. ITERATIVE ADAPTATION

In the previous sections, we explained that filters F with large gains are undesirable because this might generate problems such as control-signal saturation or loss of stability robustness. From Table I it is clear that adaptive tuning, i.e., stopping the adaptation after a finite duration, is a reasonable alternative because in the tradeoff between norm filter reduction and performance degradation, the former is significant and the latter is almost negligible. However, this compromise is not always desirable because the capability to adapt is lost, and therefore, any change in the profile of the disturbance would result in significant performance degradation. Another reason why adaptive tuning might not be desirable is that at different locations of the HDD the disturbance statistics are different.

In Section VI, we showed that frequency weighting is an effective general method to deal with the problems presented in Section V. However, in this particular case, considering the characteristics of the disturbance affecting the HDD system, another method can be attempted. The main idea is based on the observation that, as shown in Section VIII, when tuning low-order filters using the scheme in Fig. 8, the resulting tuned


 Fig. 22. Block diagram of new closed-loop plant G_1 .

 Fig. 23. Evolution of filter gains f_l over time. These gains were obtained from the experimental implementation of the first iteration of the iterative adaptation method on track 15 000 of head 0.

LTI controller mainly rejects the low-frequency content of the disturbance signal.

It is clear that for a fixed-gain tuned filter F , the scheme in Fig. 8 is equivalent to the LTI closed-loop plant shown in Fig. 22, where $U_1 = F_1(1 + \hat{G}F_1)^{-1}$ and F_1 is a filter tuned as in Section IV-B. The signal \hat{y}_1 in the LTI diagram in Fig. 22 has a low-frequency content that is significantly smaller when compared with the low-frequency content in \hat{y} in Fig. 8. Then, if we replace G with G_1 and \hat{G} with a reidentified plant \hat{G}_1 in the system in Fig. 8, the effect over the adaptive part should be similar to using high-pass frequency weighting. To see this effect, notice that under assumption (11), frequency weighting is equivalent to replacing w_1 with Hw_1 , where H is a high-pass filter.

To test the idea proposed in the previous paragraph, we implemented the system in Fig. 8 employing G_1 and \hat{G}_1 with $H = 1$. The effectiveness of this approach is demonstrated in Fig. 23. There, it is clear that the filter parameters converge and the adaptive system behaves robustly. The slight discrepancies between the experimental and theoretical steady-state gains are explained by the fact that the theoretical solution relies on identified models of the closed-loop plant and the disturbance model, and therefore, it is conceivable that the models, in this case, are not as accurate as the identified models in Section III.

The experimental results in Figs. 23 and 24 show that with this simple method, two important things are achieved. The first one is that, in this particular case, the system can be allowed to

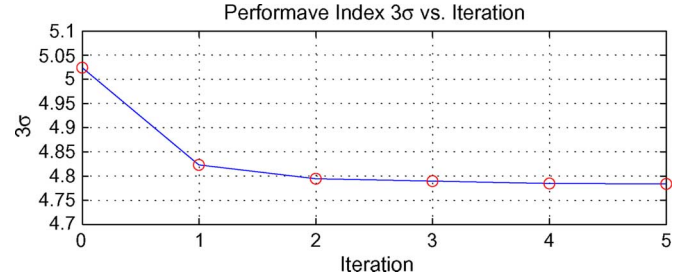


Fig. 24. Performance as function of the number of iterations. The first iteration improves the system performance significantly. The improvement achieved by the 5th iteration over the 4th one is negligible. The experiments were performed on track 15 000 of head 0.

adapt indefinitely because the steady-state filter gains f_l correspond to a filter with high-frequency gain small enough, such that, the problems in Section V do not appear. The second one is that the performance index 3σ is improved noticeable. This is explained by the facts that in presence of stationary disturbances, the adaptive controller achieves steady-state, and that in presence of non-stationary disturbances the controller adapts indefinitely.

The process described in the previous paragraph can be reproduced indefinitely, for tuning new LTI controllers, until no further improvement in performance is achieved. Repeating the process iteratively generates transfer functions G_i , $i = 1, 2, \dots$ defined as

$$G_i = P \left[1 + P \left(C - \sum_{j=1}^i U_j \right) \right]^{-1} \quad (28)$$

with $U_j = F_j(1 + \hat{G}_{j-1}F_j)^{-1}$, where F_j is a fixed-gain filter, adaptively tuned according to Fig. 8, employing the corresponding identified closed-loop plant \hat{G}_{j-1} at iteration $j - 1$. Notice that when using this method for tuning controllers, at a given iteration i , the closed-loop transfer function G_i in (28) is not explicitly computed but estimated offline using the *nAsid* algorithm according to the same procedure explained in Section III. Therefore, this method increases the computational burden of the tuning process but not the computational complexity of its real-time implementation. The improvement in performance versus iteration number is summarized in Fig. 24. There, it can be observed that a substantial improvement is achieved with the first iteration, that a moderate improvement is achieved with the second, third, and fourth iterations, and that no noticeable improvement is achieved with the fifth one. The improvement with the first iteration is explained due to the fact that F_2 reaches steady-state while F_1 is stopped before reaching steady-state.

VIII. SUMMARY OF EXPERIMENTAL RESULTS

The main purpose of this section is to show that the methods, results and ideas presented in the previous sections are valid not only for the case head 0/track 15 000, but also for the hard drive in general. This is immediately inferred from the data summarized in Table II, where the performance achieved at various locations of the HDD using various methods is shown. This comparison is relevant to the validation of the control methods,

TABLE II
PERFORMANCE INDEX 3σ OF THE POSITION ERROR SIGNAL (PES) AS PERCENTAGE OF THE TRACK WIDTH. IN ALL CASES $L = 6$

	Head 0			Head 1		
	$y_{ref} = 10\ 000$	$y_{ref} = 15\ 000$	$y_{ref} = 20\ 000$	$y_{ref} = 10\ 000$	$y_{ref} = 15\ 000$	$y_{ref} = 20\ 000$
LTI controller C	18.1429	17.2467	20.6328	16.3020	18.6647	22.6426
C + tuned F (tuning time $T = 20$ s)	5.2305	5.1433	4.9573	5.3033	5.2811	4.9583
C + tuned F (tuning time $T = 80$ s)	5.1767	5.0238	4.8593	5.2290	5.1197	4.7372
C + adaptive F with high-pass H (cutoff frequency 1.0 kHz)	5.8339	5.7916	5.4132	5.6843	5.7002	5.2829
C + adaptive F with high-pass H (cutoff frequency 1.3 kHz)	6.6063	6.5195	5.9428	6.2459	6.4904	5.6888
C + iterative adaptation (1^{st} iteration)	5.0088	4.8228	4.7827	5.0489	4.9219	4.7001

because at different locations of the HDD, the plant systems, and disturbances are significantly different. In order to have statistically comparable information, the experiments shown in Table II were conducted consecutively, therefore, those do not reflect changes in the environment. However, numerous experiments conducted under different temperature conditions confirmed the validity of the methods presented here.

A first conclusion to be extracted from Table II, is that the scheme in Fig. 8 is suitable and effective for tuning minimum-variance controllers, since the controller tuned at the location head 0/track 15 000 achieves excellent performances at different locations of the HDD. In this respect, it is important to note that the best performances displayed in Table II are substantially better than the ones achieved in the same commercial HDD, using the AQC method [5].

A second conclusion is that the fully adaptive frequency-weighting controller works robustly on all the HDD locations where it was implemented. As predicted in Section VI, there exists a clear tradeoff between the cutoff frequency of the high-pass weighting filter H and performance. A third and last conclusion is that, in this particular case, employing the iterative adaptation method is an excellent choice, since stability robustness and high performance can be achieved simultaneously. Notice that at some locations of the HDD, the 3σ value is as good as 4.7. The downside of this method is that it might not work on other systems.

Finally in this section, we graphically summarize in Fig. 25 the experimental results obtained at the location head 0/track 15 000 using an adaptively tuned filter F (plots on the left in Fig. 25), and the ones obtained using the frequency-weighting adaptive scheme (plots on the right in Fig. 25). There, the most important thing to remark is that frequency weighting allows us not only to implement fully adaptive schemes robustly, but also it allows the system to adapt fast. This is clear from the fact that when using frequency weighting, the system achieves 95% of its steady-state performance in 8 ms. It should be noted that in the cases summarized in Fig. 25, and in all the cases shown in Table II, the HDD system behaved robustly, being possible to run it for indefinite amounts of time, without the appearance of spiky or unstable responses.

IX. CONCLUSION

In this paper, we presented an analytical and experimental investigation of the main issues involved in the design and implementation of minimum-variance adaptive systems for track-following control of hard disk drives. A significant part of this work was devoted to the problems of control-signal saturation and

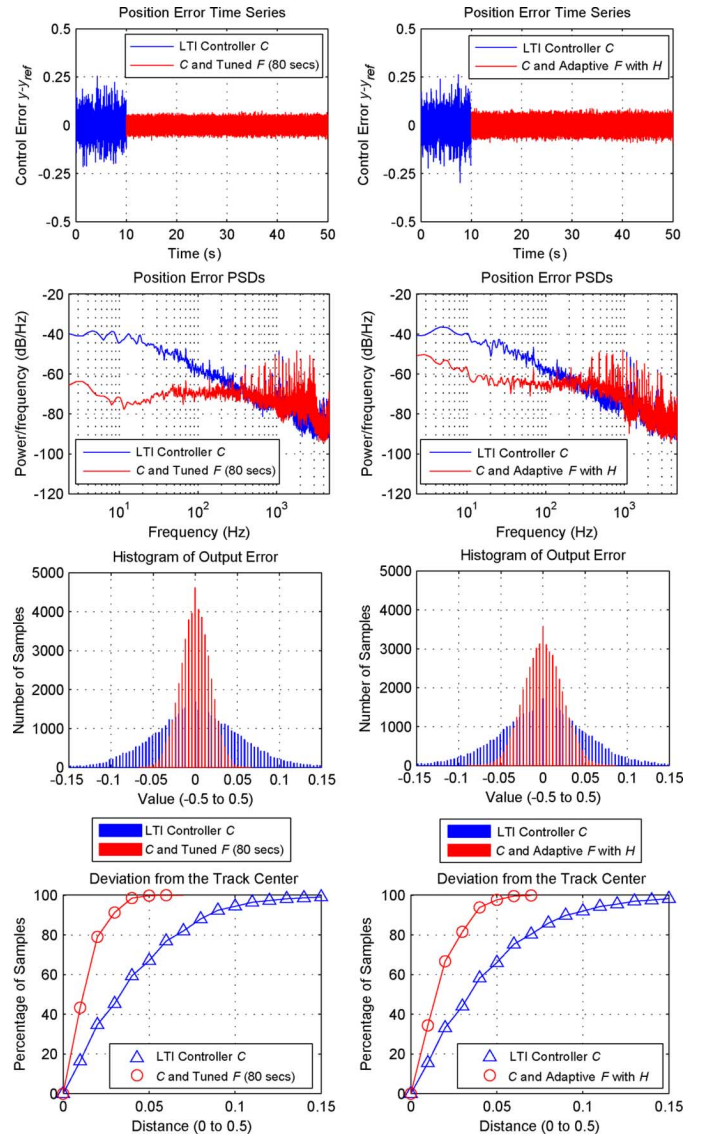


Fig. 25. Experimental results obtained at location head 0/track 15 000 using an adaptively tuned filter F (plots on the left), and the ones obtained using the frequency-weighting fully adaptive scheme (plots on the right).

loss of stability robustness, caused by the presence in the adaptive loop of prediction filters with high gains over the high-frequency range. In order to deal with these issues, we developed and implemented two methods: frequency weighting and iterative adaptation. The former is a general method first introduced in [11], the latter was demonstrated to be an excellent choice in this particular case, since it allowed us to achieve 3σ values as good as 4.7 at some locations of the HDD.

APPENDIX I

SOLUTION TO THE MINIMIZATION OF (20)

The method used in this paper is a direct extension of the solution to the classical Wiener filter problem described in [29]. The idea is to find the filter $F(z) = \sum_{l=0}^L f_l z^{-l}$ that minimizes $E\{d(k) + [Fs](k)\}^2$, with $d = W_1 \varepsilon_w$ and $s = \hat{G}W_1 \varepsilon_w$, which is equivalent to solving (20). From [29, Ch. 5], the vector f^o containing the optimal parameters is

$$f^o = \begin{bmatrix} f_0 \\ f_1 \\ \vdots \\ f_L \end{bmatrix} = -R_s^{-1} r_{ds} \quad (29)$$

where

$$R_s = \begin{bmatrix} r_s(0) & r_s(1) & \cdots & r_s(L) \\ r_s(1) & r_s(0) & \cdots & r_s(L-1) \\ \vdots & \vdots & \cdots & \vdots \\ r_s(L) & r_s(L-1) & \cdots & r_s(0) \end{bmatrix}, \quad r_{ds} = \begin{bmatrix} r_{ds}(0) \\ r_{ds}(1) \\ \vdots \\ r_{ds}(L) \end{bmatrix}$$

with $r_s(k) = E\{s(n)s(n-k)\}$ and $r_{ds}(k) = E\{d(n)s(n-k)\}$. Thus, the only thing left, is to find relations for $r_s(k)$ and $r_{ds}(k)$. In order to do that, define the transfer function Φ as the mapping from ε_w to z , with $z(n) = [d(n)s(n)]^T$, and notice that

$$E\{z(n)z^T(n-k)\} = \begin{bmatrix} r_d(k) & r_{ds}(k) \\ r_{sd}(k) & r_s(k) \end{bmatrix}. \quad (30)$$

To compute (30) consider any state-space realization of Φ given by

$$\begin{aligned} x(n+1) &= A_\Phi x(n) + B_\Phi \varepsilon_w(n) \\ z(n) &= C_\Phi x(n) + D_\Phi \varepsilon_w(n). \end{aligned} \quad (31)$$

Then, the relation

$$E\{x(n+1)x^T(n+1)\} = A_\Phi [E\{x(n)x^T(n)\}]A_\Phi^T + B_\Phi B_\Phi^T \quad (32)$$

follows immediately. Now, given that the random process $\varepsilon_w(n)$ is stationary and assuming that A_Φ is stable, it follows, as shown in [32], that $r_x(0) = E\{x(n)x^T(n)\}$ solves the discrete Lyapunov equation

$$A_\Phi r_x(0)A_\Phi^T - r_x(0) + B_\Phi B_\Phi^T = 0. \quad (33)$$

Finally, after some algebraic manipulations it is clear that

$$E\{z(n)z^T(n-k)\} = \begin{cases} C_\Phi r_x(0)C_\Phi^T + D_\Phi D_\Phi^T, & k = 0 \\ C_\Phi A_\Phi^k r_x(0)C_\Phi^T + C_\Phi A_\Phi^{k-1} B_\Phi D_\Phi^T, & k \geq 1 \end{cases} \quad (34)$$

which yields the data needed to compute (29).

REFERENCES

[1] R. Horowitz and B. Li, "Adaptive control for disk file actuators," in *Proc. 34th IEEE Conf. Dec. Control*, New Orleans, LA, Dec. 1995, pp. 655–660.
 [2] R. Horowitz and B. Li, "Design and implementation of adaptive non-repetitive track-following disk file servos," in *Proc. Amer. Control Conf.*, Seattle, WA, Jun. 1995, pp. 4161–4166.

[3] R. Horowitz, B. Li, and J. W. McCormick, "Wiener-filter-based minimum variance self-tuning regulation," *Automatica*, vol. 34, no. 5, pp. 531–544, May 1998.
 [4] A. Sacks, M. Bodson, and P. Khosla, "Experimental results of adaptive periodic disturbance cancellation in a high performance magnetic disk drive," *ASME J. Dyn. Syst., Meas., Control*, vol. 118, no. 3, pp. 416–424, Sep. 1996.
 [5] K. Krishnamoorthy and T.-C. Tsao, "Adaptive-Q with LQG stabilization feedback and real time computation for disk drive servo control," in *Proc. Amer. Control Conf.*, Boston, MA, Jun. 2004, pp. 1171–1175.
 [6] B. Widrow and E. Walach, *Adaptive Inverse Control*. Upper Saddle River, NJ: Prentice-Hall, 1996.
 [7] T.-T. Tay, I. Mareels, and J. B. Moore, *High Performance Control*. Boston, MA: Birkhäuser, 1998.
 [8] V. Kučera, *Discrete Linear Control*. Prague, Czechoslovakia: Academia, 1979.
 [9] G. C. Goodwin and K. S. Sin, *Adaptive Filtering, Prediction and Control*. Englewood Cliffs, NJ: Prentice-Hall, 1984.
 [10] A. H. Sayed, *Fundamentals of Adaptive Filtering*. New York: Wiley, 2003.
 [11] N. O. Pérez-Arancibia, J. S. Gibson, and T.-C. Tsao, "Frequency-weighted minimum-variance adaptive control of laser beam jitter," *IEEE/ASME Trans. Mechatronics* vol. 14, no. 3, pp. 337–348, Jun. 2009.
 [12] N. O. Pérez Arancibia, N. Chen, S. Gibson, and T.-C. Tsao, "Adaptive control of jitter in laser beam pointing and tracking," in *Proc. SPIE 6304, Free-Space Laser Commun. VI*, San Diego, CA, Sep. 2006, 63041G.
 [13] N. O. Pérez Arancibia, S. Gibson, and T.-C. Tsao, "Saturation and frequency weighting in adaptive control of laser beam jitter," in *Proc. SPIE 6709, Free-Space Laser Commun. VII*, San Diego, CA, Aug. 2007, 6709-27.
 [14] R. Horowitz and B. Li, "Adaptive track-following servos for disk file actuators," *IEEE Trans. Magn.*, vol. 32, no. 3, pp. 1779–1786, May 1996.
 [15] J. C. Willems, "Dissipative dynamical systems part I: General theory," *Archive for Rational Mech. Anal.*, vol. 45, no. 5, pp. 321–351, Jan. 1972.
 [16] J. C. Willems, "Dissipative dynamical systems part II: Linear systems with quadratic supply rate," *Archive for Rational Mech. Anal.*, vol. 45, no. 5, pp. 352–393, Jan. 1972.
 [17] P. Ioannou and B. Fidan, *Adaptive Control Tutorial*. Philadelphia, PA: SIAM, 2006.
 [18] L. Ljung and T. Söderström, *Theory and Practice of Recursive Identification*. Cambridge, MA: The MIT Press, 1983.
 [19] D. Abramovitch and G. Franklin, "A brief history of disk drive control," *IEEE Control Syst. Mag.*, vol. 22, no. 3, pp. 28–42, Jun. 2002.
 [20] W. Messner and R. Ehrlich, "A tutorial on controls for disk drives," in *Proc. Amer. Control Conf.*, Arlington, VA, Jun. 2001, pp. 408–420.
 [21] D.-S. Hwang, S.-C. Peng, and P.-L. Hsu, "An integrated control/diagnostic system for a hard disk drive," *IEEE Trans. Control Syst. Technol.*, vol. 2, no. 4, pp. 318–326, Dec. 1994.
 [22] Y. T. Teo and T. T. Tay, "Application of the ℓ^1 -optimal regulation strategy to a hard disk servo system," *IEEE Trans. Control Syst. Technol.*, vol. 4, no. 4, pp. 467–472, Jul. 1996.
 [23] V. Venkataramanan, K. Peng, B. M. Chen, and T. H. Lee, "Discrete-time composite nonlinear feedback control with an application in design of a hard disk drive servo system," *IEEE Trans. Control Syst. Technol.*, vol. 11, no. 11, pp. 16–23, Jan. 2003.
 [24] C. Du and G. Guo, "Lowering the hump of sensitivity functions for discrete-time dual-stage systems," *IEEE Trans. Control Syst. Technol.*, vol. 13, no. 5, pp. 791–797, Sep. 2005.
 [25] P. A. Ioannou, H. Xu, and B. Fidan, "Identification and high bandwidth control of hard disk drive servo systems based on sampled data measurements," *IEEE Trans. Control Syst. Technol.*, vol. 15, no. 6, pp. 1089–1095, Nov. 2007.
 [26] U. Forssell and L. Ljung, "Closed-loop identification revisited," *Automatica*, vol. 35, no. 7, pp. 1215–1241, Jul. 1999.
 [27] P. Van Overschee and B. De Moor, *Subspace Identification for Linear Systems*. Norwell, MA: Kluwer, 1996.
 [28] "Signal Processing Toolbox User's Guide," The MathWorks, Inc., Natick, MA, 2008.
 [29] S. Haykin, *Modern Filters*. New York: Macmillan, 1998.
 [30] K. Popper, *The Logic of Scientific Discovery*. London, U.K.: Routledge, 2002.
 [31] M. A. Dahle and I. J. Diaz-Bobillo, *Control of Uncertain Systems*. Englewood Cliffs, NJ: Prentice-Hall, 1995.
 [32] T. Kailath, A. H. Sayed, and B. Hassibi, *Linear Estimation*. Upper Saddle River, NJ: Prentice-Hall, 2000.



Néstor O. Pérez-Arancibia (S'05–M'08) received the Ingeniero and M.Eng. degrees from the Pontificia Universidad Católica de Chile, Santiago, in 2000 and the Ph.D. degree from the Mechanical and Aerospace Engineering Department, University of California, Los Angeles (UCLA), in 2007.

Since October 2007, he has been a Postdoctoral Scholar with the Laser Beam Control Laboratory and also with the Mechatronics and Controls Laboratory in the Mechanical and Aerospace Engineering Department, UCLA. His current research interests include feedback control, adaptive filtering, adaptive optics, and mechatronics.



Tsu-Chin Tsao (S'86–M'88–SM'09) received the B.S. degree in engineering from National Taiwan University, Taiwan, in 1981, and the M.S. and Ph.D. degrees in mechanical engineering from The University of California, Berkeley, in 1984 and 1988, respectively.

In 1999, he joined the faculty of UCLA, where he currently is a Professor in the Mechanical and Aerospace Engineering Department. He served 11 years on the faculty of the Mechanical and Industrial Engineering Department, The University

of Illinois, Urbana-Champaign. His research interests include control systems and mechatronics.

Dr. Tsao was a recipient of the *ASME Journal of Dynamic Systems, Measurement, and Control* Best Paper Award for the papers published in the journal in 1994, the Outstanding Young Investigator Award from ASME Dynamic Systems and Control Division, in 1997, and Hugo S. Shuck Best Paper Award from American Automatic Control Council, in 2002.



James S. Gibson (M'08) received the B.S. degree in aerospace engineering, the M.S. degree in engineering mechanics, and the Ph.D. degree in engineering mechanics from The University of Texas at Austin, in 1970, 1972, and 1975, respectively.

In 1977, he joined the faculty of the University of California, Los Angeles (UCLA), where he currently is a Professor of Mechanical and Aerospace Engineering. He served on the faculties of the Aerospace Engineering and Engineering Mechanics Department, The University of Texas at Austin and the

Engineering Science and Mechanics Department, Virginia Polytechnic Institute and State University, Blacksburg. His research interests include control and identification of dynamical systems and adaptive filtering, with applications to identification and control of flexible structures, control of laser beams and adaptive optics, identification and control of micro inertial sensors, control of fluid flow and noise control.

Dr. Gibson has served as an Associate Editor for the *SIAM Journal on Control and Optimization* and for the IEEE TRANSACTIONS ON AUTOMATIC CONTROL.